Noncontact measurements of residual stress distribution and grain size in titanium alloys with laser ultrasonic system

Santhakumar Sampath[1], Zheng Zhang[1], Zi Wen Tham[1], Yi Fan Chen[1], Debbie Hwee Leng Seng[1], Thulsiram Gantala[2] and Lei Zhang[1*]

[1]Institute of Materials Research and Engineering (IMRE), Agency for Science, Technology and Research (A*STAR), 2 Fusionopolis Way, Innovis #08-03, Singapore 138634, Republic of Singapore

[2]Department of Mechanical Engineering, Indian Institute of Technology Madras, Chennai, 600036, India

***** Corresponding author

Abstract

In this study, a laser ultrasonic system is proposed for nondestructive evaluations of both the residual stress depth profile and grain size in titanium alloy materials (grade Ti-6Al-4V) processed by warm shot peening (WSP). The method utilizes a pulsed laser to generate a surface acoustic wave (SAW) along the cross-section of the sample, and a laser interferometer to detect the SAW signals. The uniqueness of the proposed system includes the followings: (i) the capacity to measure and locate the maximum compressive residual stress (CRS), (ii) a high spatial resolution of 30 μm, which facilitates precise extraction of the residual stress profile and grain size, (iii) a more effective approach for estimating grain size through the frequency shift model developed and (iv) the ability to analyze both residual stress and grain size in a single measurement. A theoretical model for measuring the residual stress profile is described, along with a model built to correlate the center frequency shift and mean grain size of the sample. Laser ultrasonic measurements were performed in samples treated by WSP at different temperatures (32 °C, 100 °C, 200 °C and 300 °C). The results obtained by the laser ultrasonic method are compared to those obtained by X-ray stress measurement, center-hole drilling (CHD), and electron backscattering diffraction (EBSD).

Key words: Laser ultrasonic; Residual stress profile; Grain size; Titanium alloy; Warm shot peening; X-ray stress measurement

1. Introduction

Titanium alloys are commonly used in aerospace applications due to their excellent properties such as good ductility, high strength and excellent corrosion resistance [1-3]. However, due to stress concentration, the mechanical/thermal cyclic loading can accelerate the initiation rate of fatigue cracks and thereby leads to a premature failure of material. Studies have shown that fatigue cracks typically begin in the surface layers of the components and are very sensitive to microstructure [4, 5]. In engineering, it is possible to effectively suppress the initiation and propagation of fatigue cracks by introducing residual stress and grain refinement (GR) [6] [7].

Surface treatment techniques, such as shot peening (SP) [8, 9], laser shot peening [10], waterjet peening [11], and hammer peening [12], extensively employed to introduce compressive residual stress (CRS) and GR in the near-surface regions of materials. Among these techniques, SP is the most well-established and cost-efficient approach [13, 14]. The surface treatment is performed by blowing a huge number of small and hard particles (shots) onto the surface of the component, thus causing the plasticization of the surface layer [15, 16]. As a result of this process, CRS is introduced and the micro-structure in the surface region of the components is refined. CRS on the surface effectively closes any short cracks formed during SP, thereby enhancing fatigue life. In addition to CRS, uneven plastic deformation on the surface and sub-surface can give rise to GR to a certain depth [17]. Studies have shown that the GR is another important factor in improving component fatigue performance, as it restrains crack initiation and hinders crack propagation [18-20].

Conventional SP typically improves fatigue performance to a depth of 150-250 μm. To increase the depth of plastic deformation and enhance the properties of the surface layer, SP has been attempted at elevated temperatures for spring steel [21] and Ti64 alloys [22] with some success, and has been termed as warm-shot-peening (WSP). By subjecting the component's surface to WSP, plastic deformation is induced near the surface, resulting in the generations of CRS and GR. The CRS and GR generated by WSP play an important role in the improved fatigue performance and hardness of the peened components [23]. Therefore, it is of great significance to investigate the residual stress profile and grain size distribution to estimate the mechanical strength and to assess the fatigue performance of the components.

Various methods can be utilized to determine the microstructure features of materials, including X-ray diffraction (XRD) [24], neutron diffraction [25, 26], electron backscatter diffraction (EBSD) [27, 28], center-hole drilling (CHD) [29], and ultrasonic [30, 31]. XRD and neutron diffraction, popular non-destructive methods, involve scanning the sample at multiple tilt angles to calculate residual stress based on d-spacing changes [32]. However, these methods have limitations such as low penetration depth (<10 μm, depending upon materials) and high cost of measurement. Recent studies have demonstrated that using x-ray diffraction and layer removal (e.g., via electropolishing) can provide an accurate estimation of residual stress [33-35]. Nevertheless, stress calculation can be affected by errors stemming from stress relaxation due to the chemical etching step utilized in the layer removal process. EBSD [36-38] is the most well-known characterization method, due to its high resolution, both spatial (< 10 nm) and angular (< 1°) [39]. Despite its advantages, the method is associated with a high cost of system, operation and maintenance. Additionally, the samples are subject to stringent restrictions on size and surface finishing. The CHD method involves using a strain gauge sensor to measure through-thickness residual strain via incremental hole drilling across depth [40, 41] . In many research works, the CHD method is combined with the other methods to reliably estimate the residual stress [42-45]. For instance, the combination of CHD and XRD is employed to determine the residual stresses in ultrafine-grained laminated metal composites [46].

Ultrasonic method for evaluating the microstructures is considered the most feasible nondestructive method [47, 48]. Laser-based ultrasonic methods, in particular, offer advantages such as non-contact, high-speed, and cost-effective [49-51]. Sanderson et al. [52] investigated the relationship between the velocity of laser-induced surface acoustic wave (SAW) and the distribution of residual stress. However, this approach is not suitable for estimating stress profiles within the thickness of materials. Duquennoy [53] utilized laser ultrasonic measurements to analyze residual stress in steel samples subjected to different heat treatments. The acoustoelastic theory was employed to calculate residual stress in aluminum samples treated with low plasticity burnishing [54]. Ruiz et al. [55] discussed the dispersion of SAW caused by residual stress and developed a diffraction correction approach to improve the accuracy of SAW measurements. However, current applications of laser ultrasonic methods primarily focus on measuring the average residual stress of materials. There is a lack of studies that measure the depth profile of residual stress in materials using laser ultrasonics.

Besides providing information about residual stress, SAW can also be used to probe materials' microstructure at the same time, as their propagation characteristics within a particular material are influenced by the material's microstructure [56]. The ultrasonic velocity [57], the backscattering [58] and the ultrasonic attenuation [59] methods have been widely used to evaluate grain size of the material. The accuracy of grain size determination using the ultrasonic velocity method may be limited due to its low sensitivity to changes in grain size. The backscattering method determines the average grain size based on the correlation with the backscattering coefficient [60]. However, it becomes less effective for materials with large grain sizes. The attenuation method compares the amplitudes of successive back-wall echoes to determine grain size feasibility [61]. However, it is challenging to identify the contribution of grain scattering and other factors like dislocation and absorption, which can affect the accuracy of grain size estimation [62]. Recently, spectral analysis methods have shown promise for improving grain size evaluation in materials with strong scattering or coarse grains due to its insensitivity to reflection, transmission effects, and ultrasonic signal accuracy [63, 64]. However, only a few studies [63, 65] have explored the correlation between grain size and the center frequency of SAW.

Therefore, the GR and grain size as a function of depth are evaluated based on laser ultrasonic method in this study. The uniqueness of the proposed method includes the followings: (i) capability for measuring and locating the maximum CRS, (ii) a high spatial resolution of 30 μm, allowing for precise extraction of the residual stress profile, (iii) more effective estimation of gran size through the frequency shift model developed and (iv) analyzing both residual stress and grain size at a single measurement. Experimental-wise, the SAW signals were firstly collected by laser ultrasonics from the cross-sections of the samples shot peened at different temperatures (32 °C, 100 °C, 200 °C and 300 °C). The relative velocity change and center frequency shift of the SAW were then calculated to evaluate the residual stress profile and grain size, respectively. Finally, to validate the performance of the laser ultrasonic method, the surface microstructures were benchmarked against the results from X-ray stress measurement, CHD, and EBSD.

2. Material and methods

2.1 Sample preparation and warm shot peening process

The five test samples used in this study were made of commercial-grade Ti-6Al-4V (Ti64). No heat treatment was performed on the intact sample prior to the SP. Each sample had a dimension of 50 mm × 30 mm × 10 mm as shown in Fig. 2(a). The pictures of Ti64 before and after SP at 32, 100, 200 and 300 ºC are shown in Fig. 2(b). Shot peening was carried out using a duckbill nozzle set 4" above the sample surface with high-hardness cast steel as shot balls (average diameter of

340 μm). The compress air was set at 241.3 kPa. The nozzle was swiped at a speed of 0.0254 m/s for 7 strokes across the entire surface to achieve a coverage of 125% and a target intensity between 6 and 9 A. 3 ~ 5 pieces of type A Almen strip were used to verify that the intensity was stabilized prior to peening on the samples. Ti64 coupons were placed on top of a hotplate and heated to the target temperature (100 °C, 200 °C and 300 °C) before the shot-peening started. The entire hotplate was covered by a protective box, which together with other design details can be found from our earlier publication [22].

(a) (b)

Figure 1. Sample details: (a) the dimension of the sample and (b) pictures of Ti64 samples before and after peening at different temperatures.

In the current study, a hotplate-based in-situ heating system was developed for performing shot-peening in a traditional booth at different temperatures (32 °C, 100 °C, 200 °C and 300 °C). Two adaptors were designed in order to fix the samples to the hotplate during peening process, as described in [22]. The adaptors were designed to reduce the heat transferred from the hotplate to the surrounding protective cover through the samples. It is important to securely hold the samples while they experience strong impacts from the shot metals introduced by compressed air at a pressure of 241.3 kPa. Prior to carrying out the WSP process, the temperature of the sample surface was measured using a thermocouple and observed for 5 minutes to ensure stability. Peening was performed on only one side of the sample at temperatures ranging from 32 to 300 °C.

2.2 SAW measurements

The experimental setup of laser ultrasonic system for SAW measurement is demonstrated in Fig. 3. A pulsed Nd:YAG laser (NL301G, Ekspla, Lithuania) was used to generate SAW waves on the cross-section of the sample. The laser operated at a wavelength of 1064 nm, with a repetition rate of 20 Hz and a pulse duration of 5.4 ns. A pulsed laser energy of 5 mJ is incident on the sample surface to generate SAW in the thermoelastic regime using a neutral filter [66]. The laser pulse was focused into a spot with a diameter of about 10 μm by using a focus lens. The size of the laser spot determined the bandwidth of the SAW [67]. The generated broadband SAW was detected using laser interferometer system (TEMPO, Bossa Nova Technology) with a bandwidth of DC-1GHz. The interferometer system operates at a wavelength of 532 nm with a maximum power output of 1500 mW. The pitch-catch mode was employed for generating and detecting the SAW on the same side of the sample. To scan the sample in the vertical direction, a linear mechanical stage with a minimum step size of 1 μm was used. A digital oscilloscope (Tektronix Dpo4102) with a sampling rate of 4 GS/s, was used to store the signals obtained from the laser interferometer system. In order to improve the signal-to-noise ratio, 512 signals were averaged.

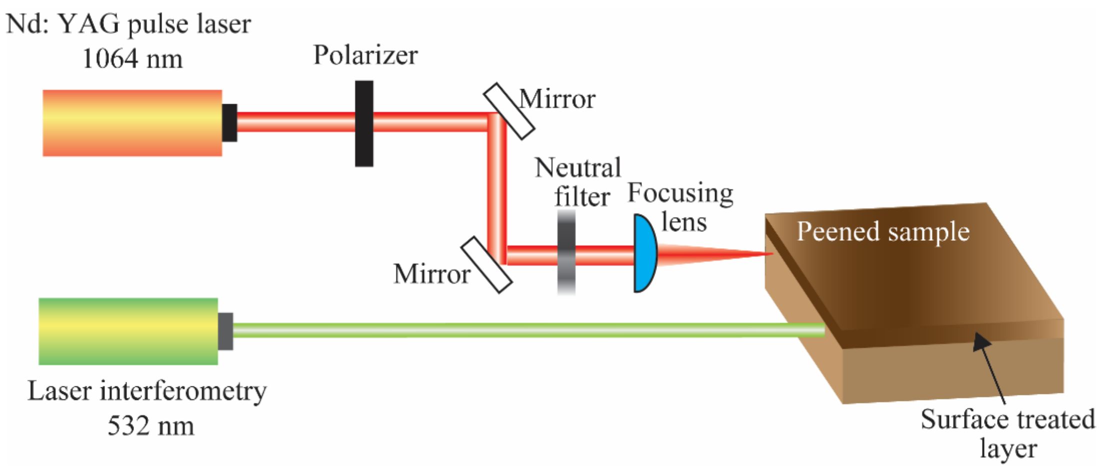

(a)

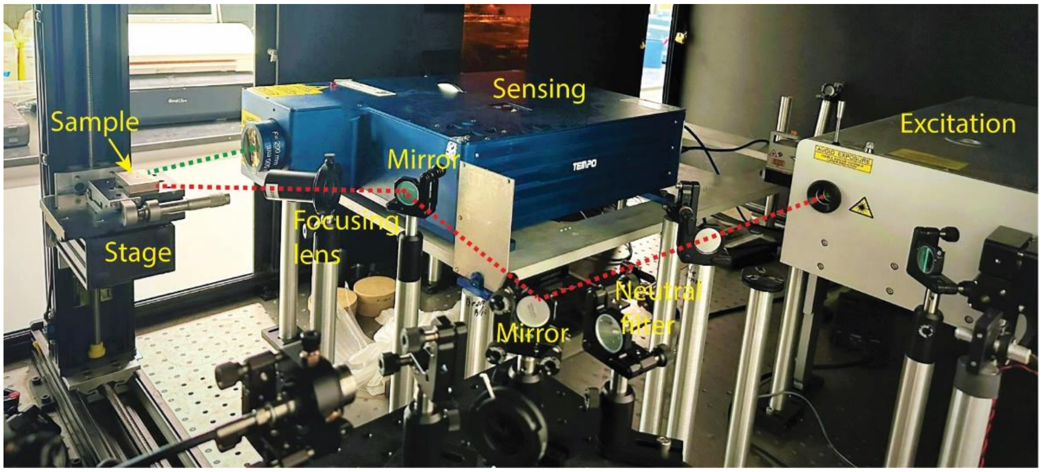

(b)

Figure 2. (a) Schematic and (b) actual photographic of the laser ultrasonic system for generation and detection of SAW.

2.3 Laser acoustic measurement strategy

The laser excitation source moves with a resolution of 30 μm along the cross-section from near-surface layer to the bulk layer. At each position $\mathrm{E_i}$ ($\mathrm{E_1, E_2 \ldots . E_n}$), a SAW is produced, and its corresponding detection points are measured at $\mathrm{S_i}$ ($\mathrm{S_1, S_2 \ldots . S_n}$) and $\mathrm{D_i}$ ($\mathrm{D_1, D_2 \ldots . D_n}$) as shown in Fig. 4. To measure the propagation time of the SAW between two positions (from S to D), the SAW is initially measured at position $\mathrm{S_1}$, with the laser interferometer system then moved sequentially at position $\mathrm{D_1}$. In this way, the residual stress profile and grain size are estimated by measuring the variation of SAW velocity and frequency centroid as a function of depth.

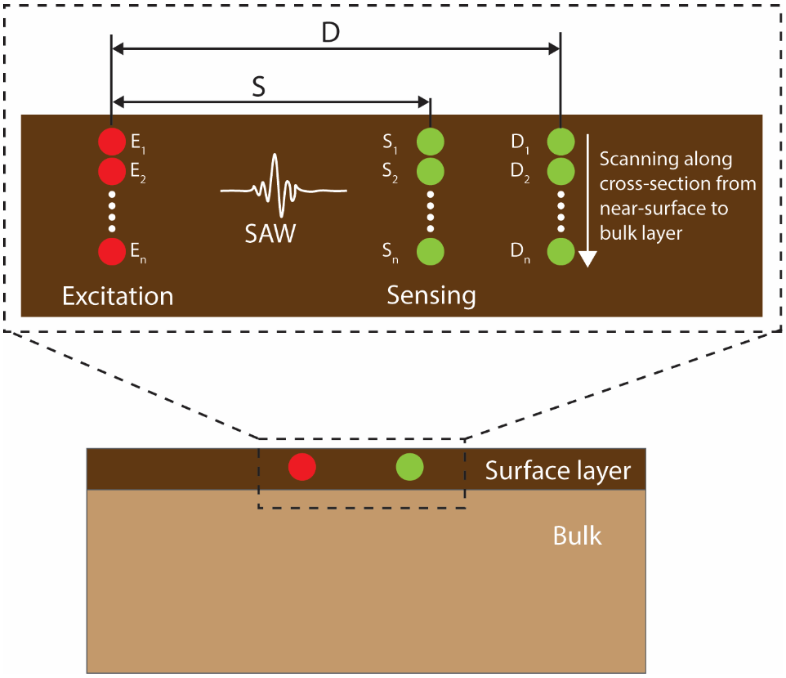

Figure 3. Positions and scanning directions of the laser ultrasonic measurements.

2.4 Other experimental details

The samples were further analyzed to investigate various properties, including the surface roughness. For metallography characterization, the JEOL 7600F field emission scanning electron microscope (FE-SEM) equipped with an EBSD detector was utilized. EBSD analysis was performed on the cross-sectional surface of the sample to determine the grain orientations and analyze the depth of deformation resulting from WSP. The residual stress on the surfaces of samples was determined using the sin2ψ method with Cu Kα X-ray (λ = 1.54 Å) and Ni filter in X-ray stress measurement (Stresstech Xstress G3). This method provides a fast and non-destructive evaluation of the residual stress at the surface to compare the effectiveness of warm shot peening at different temperatures. The CHD method utilized strain gauges to identify residual stress at different depth of the samples upon drilling inside the samples [22]. To determine the elastic constants of the Ti64 samples, a nano-indentation system (Agilent G200 Nanoindenter XP) was utilized. Indentations were made on cross-sectional samples using a Berkovich diamond tip, reaching depths of up to 1 μm. Each line scan started with an initial indentation point located 20-35 μm away from the surface, followed by four indentation points spaced 30 μm apart, and then ten points spaced 100 μm apart.

3. Results

3.1 Residual stress profile distributions

In the initial experiment, both intact and peened (WSP @ 300 °C) samples were investigated at a propagation distance (between S to D, Fig. (4)) of 30 mm from laser excitation. The difference in amplitude induced by the residual stress is difficult to discern directly from the time-domain responses (Fig. 5(a)). The wavelet spectrum was performed on a narrow time window with a duration of approximately 3.3 μs (Fig. 5(a)) using a Gaussian model as shown in Fig. 5(b). The SAW exhibited a broadband frequency range spanning from 1 to 50 MHz, with a central frequency component around 20.5 MHz. Furthermore, the amplitude of the central frequency component is larger for the peened sample than for the intact sample due to the nonlinearity of residual stress.

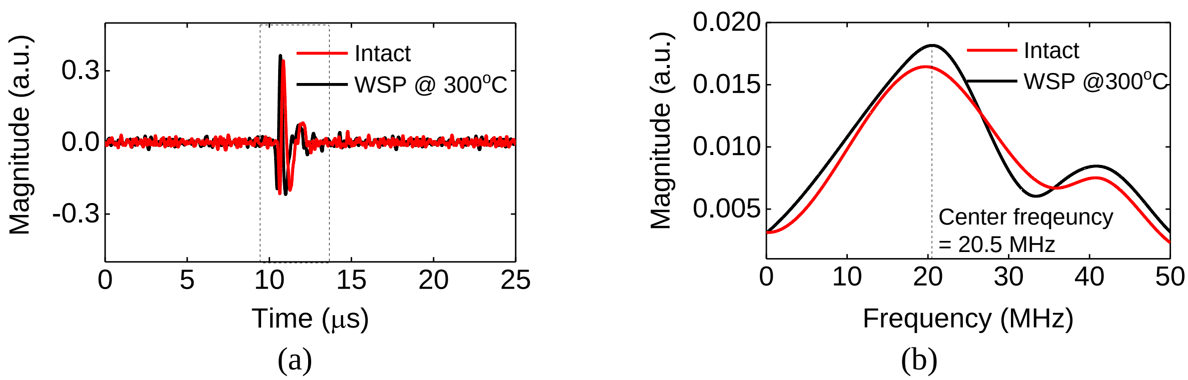

Figure 4. Results of laser ultrasonic showing (a) Time-domain responses and (b) wavelet spectra of SAW from both intact and peened (WSP @ 300°C) samples.

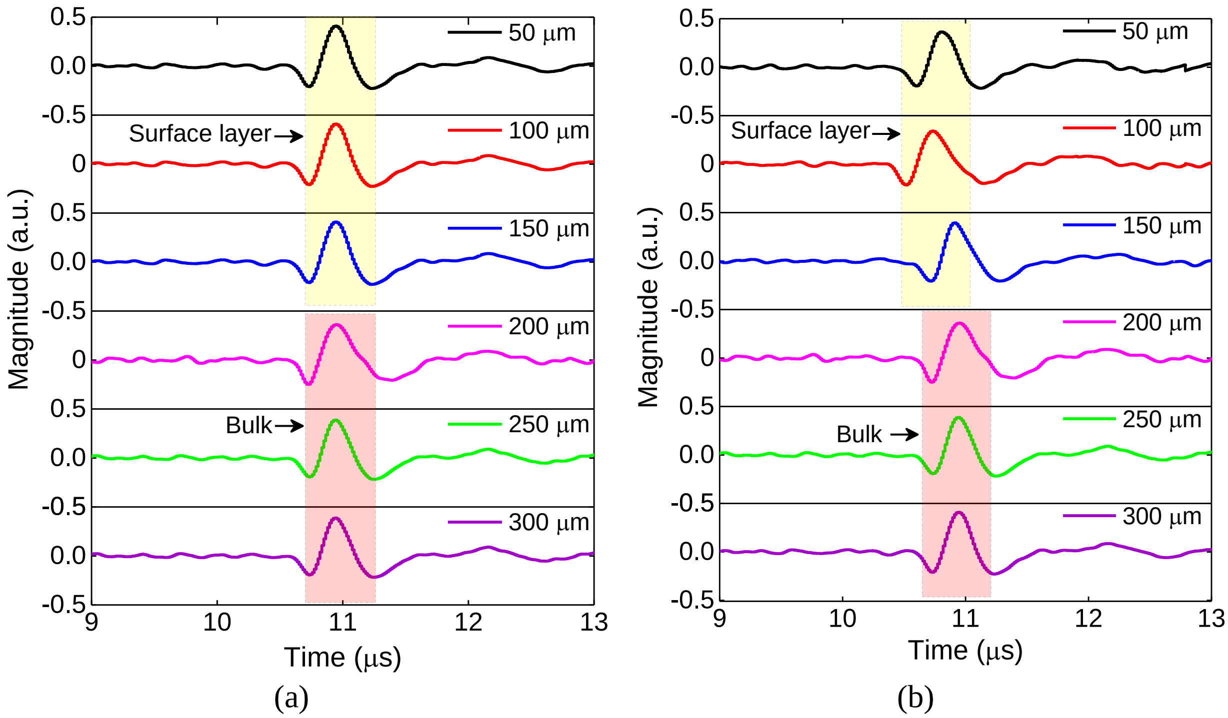

Figure 5. Time-domain responses of SAW as a function of layer depths. (a) intact and (b) peened samples (WSP @ 300 °C).

Figure 6 depicts the time-domain responses for different layer depths (50 μm, 100 μm, 150 μm, 200 μm, 250 μm and 300 μm) in intact and peened samples. The results indicate that in the intact sample, the time of flight remains constant regardless of layer depth. However, the time of flight in the peened sample initially decreases as the layer depth increases up to 100 μm, but then increases between 100 μm and 150 μm. This suggests that the change in SAW velocity is primarily influenced by the layer with CRS in the peened sample. Beyond 150 μm, the time of flight remains approximately constant suggesting no significant contribution from residual stress. Figure 7 shows the relative variations of SAW velocity ($\Delta V_{11}/V_{11}^{r}$) with different warm-shot-peened Ti64 samples, after measuring SAW's propagation time (similar in Fig. 6). It reveals that although peening took place at different temperature from room temperature (32 °C) to 300 °C, the SAW velocity profiles with depth exhibit similar patterns. They increased from 0 to a peak value of 0.025 ~ 0.030 around 100 μm (corresponding to CRS), before they lowered down to negative value of −0.005 ~ −0.008

(corresponding to tensile residual stress) around 200 ~ 350 μm and eventually returned back to zero stress state in the bulk (> 400 μm). However, the magnitude of SAW increases from 0.022 to 0.031 as the WSP temperature increases from 32 °C to 300 °C. Furthermore, the relative variation of SAW velocity demonstrates an almost linear relationship with increasing WSP temperature. This finding suggests that SAW velocity can potentially be used as an indicator for determining the residual stress depth profile of engineering structures. According to Fig. 7, the maximum magnitude of SAW velocity is observed at depths ranging from 40 to 80 μm.

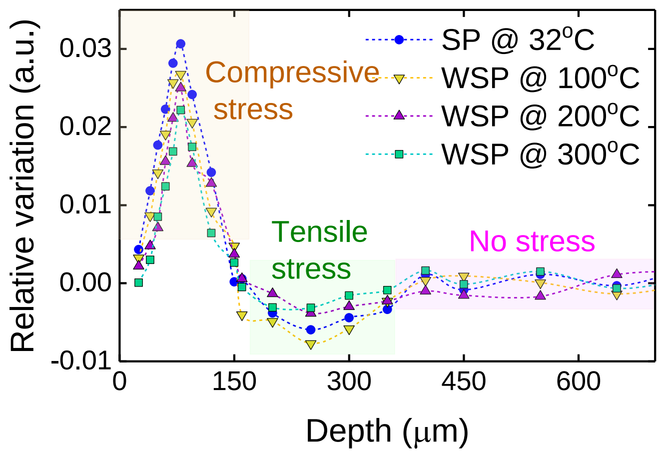

Figure 6. Relative variations of SAW velocities versus the layer depths for the sample shot-peening at 4 temperatures. The inset shows a zoom-in of the maximum SAW velocity for the 4 samples.

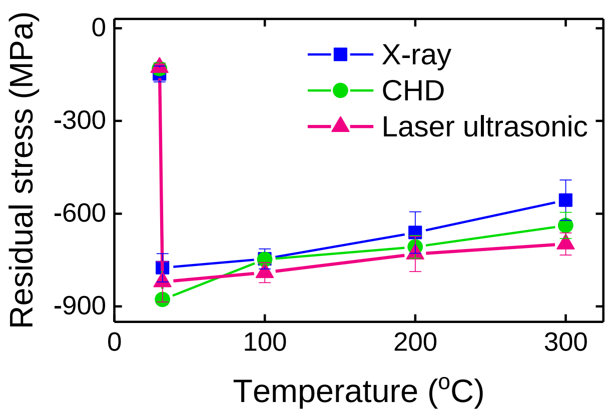

Figure 7. Comparison of maximum compressive residual stress (CRS) at the surface measured by X-ray, CHD and laser ultrasonic methods after warm shot peening treatment at 100, 200 and 300°C. The CRS values from as-received Ti64 and after shot peening at room temperature have also been included for reference

After converting the maximum SAW velocity into residual stress using Eq. (B6), the peak residual stress determined by the laser ultrasonic method for the 4 samples can be seen in Fig. 8. The peak residual stresses measured by CHD method as well as the surface residual stress by X-ray stress measurement from earlier study [22] for each sample were also included for comparison. Although X-ray stress measure only picks up surface residual stress, while CHD and laser acoustic present the maximum CRS value, the overall stress profiles obtained by these three methods are considered to be consistent (Fig. 8): the residual stresses were maximum after peening at room temperature and decreased monotonically with an increase of WSP temperature.

Table 1. The compressive residual stress of various peened samples for each method.

Samples	X-ray		CHD		Laser ultrasonic	
	CRS (MPa)	Depth (μm)	CRS (MPa)	Depth (μm)	CRS (MPa)	Depth (μm)
Intact @ 30 °C	−148.05	12	−130.62	8	−127.11	30
SP @ 32 °C	−775.02	12	−877.66	24	−820.59	30
WSP @ 100 °C	−746.31	12	−747.84	24	−790.97	30
WSP @ 200 °C	−661.01	12	−707.52	24	−730.33	30
WSP @ 300 °C	−556.37	12	−638.19	24	−698.03	60

The residual stress obtained from the laser ultrasonic method for WSP samples at 32 °C, 100 °C, 200 °C, and 300 °C are −820.59 MPa, −790.97 MPa, −730.33 MPa, and −698.03 MPa, respectively (Table 1). The values show some degree of variation among different methods, mainly due to differences in their measurement depths. Specifically, the proposed method measures the peak residual stress at a depth of 50 μm, which is deeper compared to the CHD method (40 μm). The peak residual stress values of the peened sample are significantly larger than the residual stress of the intact sample (−127.11 MPa), which was measured using the laser ultrasonic method. The residual stress in the intact sample was generated due to the grinding process [22]. When the samples were subjected to SP at 32 °C, the CRS increased substantially to −820.59 MPa. However, as the temperature increased to 100 °C, there was a slight decrease in residual stress to −790.97 MPa, indicating stress relaxation when the sample was heated up. The stress relaxation became more pronounced as the WSP temperatures rose to 200 °C and 300 °C, with the residual stress decreasing monotonically to −730.33 MPa and −698.03 MPa, respectively.

3.2 Microstructural investigations

The time-domain response and its wavelet spectrum at different propagation distances of 30 and 40 mm for the peened sample (WSP @ 300°C) are shown in Fig. 9. The results show a reduction in the magnitude of the SAW and a marginal shift in the spectrum towards lower frequencies as the propagation distance increases. The results also indicate that the center frequency of the signal for the propagation distance of 30 mm is 20.5 MHz and that of propagation distance of 40 mm is 19.2 MHz. This input frequency shift is attributed to the presence of GR in the wave propagation path. A higher average grain size is associated with increased attenuation at high frequencies, resulting in a larger downward shift in the centroid of the signal's spectrum as it propagates.

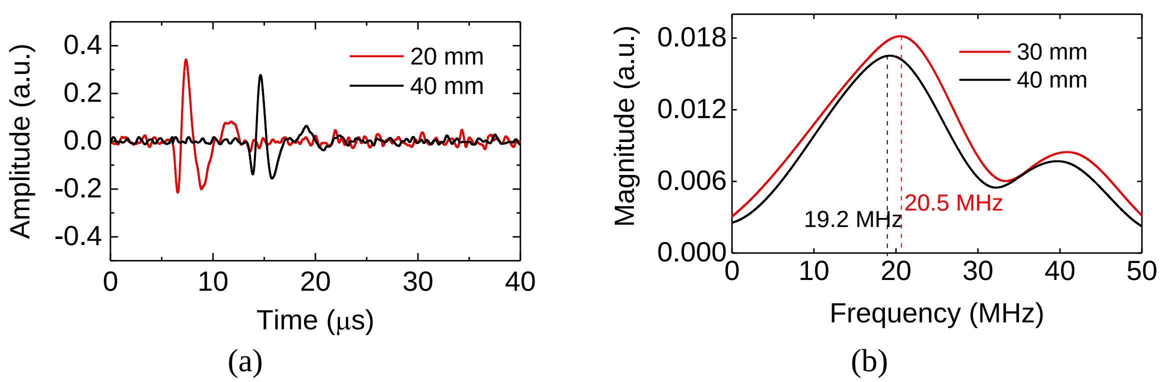

Figure 8. Laser ultrasonic measurements at different propagation distances for a peened sample (WSP @ 300°C). (a) Time-domain responses at propagation distances of 30 mm and 40 mm, (b) its corresponding frequency spectra.

The SEM images of sample surfaces after different peening processes were shown in Fig. 10. All the four surfaces were decorated with craters, indicating plastic deformation at the surface layer after peening. The surface roughness was determined using surface profiler and found to increase from 1.34 μm at 32 °C to 2.93 μm at 300 °C. The higher roughness can be attributed to a decrease in flow stress and a greater degree of plastic deformation as the samples were subjected to higher temperatures.

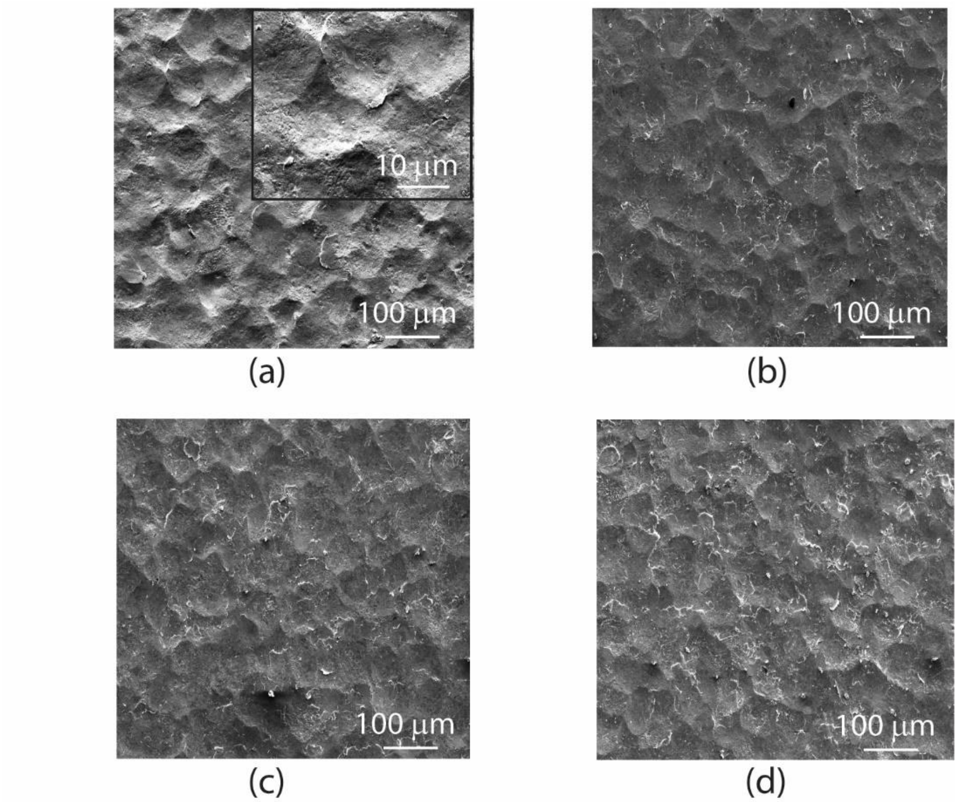

Figure 9. Surface morphology of various peened samples: (a) SP @ 32 ^{o}C (1.34 μm), (b) WSP @ 100 ^{o}C (1.77 μm), (c) WSP @ 200 ^{o}C (2.67 μm) and (d) WSP @ 300 ^{o}C (2.93 μm). The inset in (a) shows a higher magnification image of the peened surface.

Table 2. Mean grain size estimation by the proposed method compared to EBSD measurement results.

Samples	EBSD (μm)	Laser ultrasonics (μm)
Intact	15.0	40.5
32 ^{o}C	20.8	38.6
100 ^{o}C	16.7	32.0

200 ^oC	17.8	31.5
300 ^oC	18.9	28.7

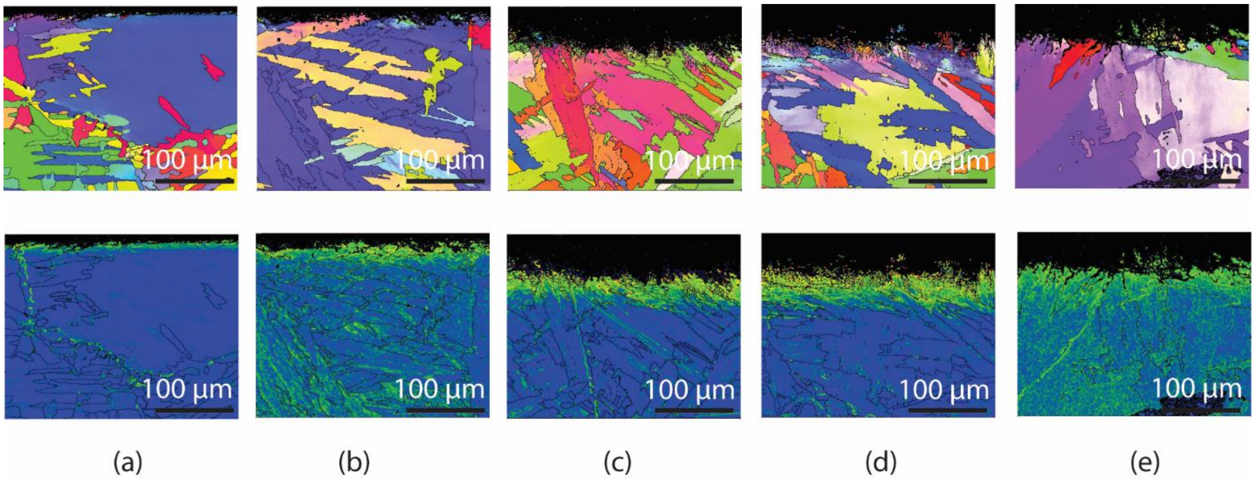

Figure 10. EBSD grain orientation maps (1st row - inverse pole figures and 2nd row - Kernel average misorientation figures) of the samples with different peening processes. (a) Intact and peening at (b) 32, (c) 100, (d) 200 and (e) 300 ^oC.

After SP treatment, the grain sizes of the surface layer have significantly reduced, as indicated by the black un-indexed regions below top surface of each sample. The black regions imply that the grains in the top surface region have been fragmented into size far less than the step size of EBSD analysis (1 µm, Fig. 11) and unable to be indexed. Furthermore, the grain size is distributed along a gradient from the surface layer to the matrix with a trend of increasing grain size with depth. According to our results, increasing the severity of the peening process by increasing temperature enhances the depth of the deformed layer as measured from the surface. Based on the Kernel average misorientation images, the cross-section of the Ti64 material can be divided into three layers: a top layer with very fine grains shown as the black region in EBSD, a middle layer (green regions) with refined grains, and a bulk layer (blue region) with the original grain size. The first two layers are formed due to the peening process. The temperature during the peening process influences the thickness of the fine grain layer. At a temperature of 32 °C, the fine-grained layer measured approximately 24.4 μm, calculated from the EBSD image (Fig. 11). As the temperature for WSP increased to 300 °C, the thickness of the black layer and fine-grained layer expanded to around 83.2 μm. The comprehensive phase composition and grain size of the sample at the four shot-peening temperatures can be found in our earlier publication [22].

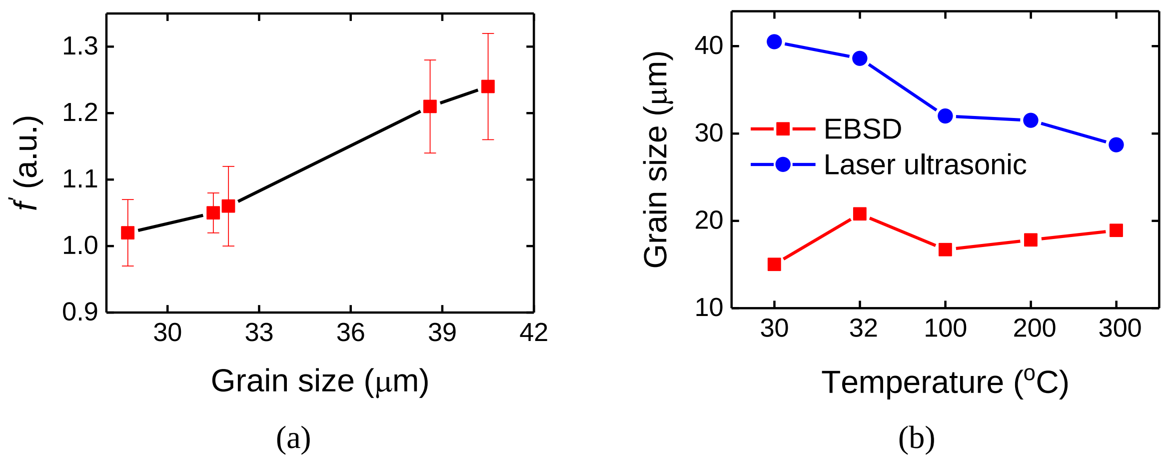

Figure 11. (a) Relationship between the center frequency ratio and mean grain size and (b) comparison of estimated grain size of the proposed method and EBSD.

Furthermore, the center frequency ratio ($f' = f_{c1}/f_{c2}$) analysis was conducted using Eq. (C4) to assess the mean grain size between successive propagation distances. Figure 12 shows the relationship between the center frequency shift ratio and the mean grain size. The error bars indicate standard deviations from five repeated measurements on the same sample. The findings reveal that samples with larger mean grain sizes demonstrate higher center frequency ratios. Additionally, larger mean grain sizes correspond to increased attenuation at high frequencies, leading to a more pronounced frequency shift in the center frequency with increasing propagation distance. These results demonstrate the effectiveness of the center frequency shift ratio for evaluating grain size with laser ultrasonics. We further compared results with our proposed method to metallographic measurements taken through SEM-based EBSD analysis (Table 2). This comparison yields a minimum error of 38.1% in grain size for the intact sample. By contrast, the experimental error for the peened sample (SP @ 32 ^{o}C) with a smaller mean grain size increased significantly to be greater than 60%.

4. Discussion

Although much progress has been made in the accuracy of nondestructive evaluation (NDE) of residual stress and grain size, there are still many difficulties, especially with non-contact characterization ultrasonic methods [68, 69]. Most ultrasonic methods can only estimate the average residual stress [70-72]. Measuring depth profile of stress in peened samples is still challenging due to the maximum stress typically being within 100 μm of the surface. Furthermore, the classical power law relationship of attenuation with grain size does not take into account the effect of grain size distribution on ultrasonic attenuation [64, 73]. For example, log-normal distribution of grain sizes, which would reduce the frequency dependence of attenuation. These factors may lead to low accuracy when estimating residual stress and grain size using ultrasonic waves. Taking all factors into account, the accurate estimation of residual stress profile and the low error of grain size evaluation in this study are attributed to the following points. The centroid frequency shift approach for grain size characterization is advantageous as it is insensitive to wave diffraction, reflection, transmission, and the laser ultrasonic system's stability. The attenuation coefficient due to grain scattering can be estimated without the influence of geometric spreading. Moreover, the effects of grain size distribution on ultrasonic wave attenuation were quantitatively examined when two critical parameters were evaluated: (1) the power law dependence of the attenuation on frequency and (2) the linear proportionality coefficient. Accurately evaluating these two parameters ensured the accuracy of grain size evaluation in this study.

When the in-situ WSP temperature was raised from room temperature to 100°C (Fig. 8), the CRS measured by proposed laser ultrasonics, CHD and X-ray stress measurement, immediately decreased in the top 52 μm layer. Further increasing the temperature of the WSP to 200 and 300°C caused a significant decrease in the CRS (Fig. 8), even though 300°C is much lower than the recrystallization temperature of Ti64. The surface CRS was slightly relieved by the in-situ WSP at 100°C, but the WSP at room temperature resulted in a larger CRS at a depth of 56 μm onwards. The CRS decreased to zero at a depth of around 350 μm compared to 210 μm after SP at room temperature (Fig. 8).

Besides introducing residual stress and GR, the peening process also tends to increase the surface roughness of a material (Fig. 10), a phenomenon commonly observed in steel [21] and Mg alloy [74]. This increase in roughness can be attributed to the thermal softening effect, which results in a reduction of hardness. Thermal softening, in turn, facilitates deformation by slip, as well as dislocation migration and dislocation annihilation at elevated temperatures. Consequently, dynamic recrystallization occurs, allowing small grains to grow into larger ones (Fig. 12(a)), provided that the WSP temperature surpasses the recrystallization temperature of the metal [75]. For instance, when subjecting Mg AZ31 to WSP at 240 and 360 °C, it led to the formation of larger grains measuring 9.2 and 13.2 μm, respectively, in contrast to the grain size after SP at room temperature (3.6 μm) [74]. The observed increase in grain size following WSP of Mg AZ31 alloys strongly indicates significant dynamic recrystallization during the WSP process.

The high estimation error (Fig. 12(b)) of mean grain size from the proposed laser ultrasonic method is likely due to three possible reasons. The primary source is attributed to the limitations of SAW frequency. To address this issue, future study aims to improve grain size estimation accuracy by combining high-frequency SAW generation with an optical interferometer system. The secondary source is attributed to different direction of measurement. The SAW measures grain size parallel to the surface, while our current sample preparation for EBSD detects grain size perpendicular to the surface plane. The third source likely arises from the limited numbers of grains within EBSD scans to provide a representative grain size information. Due to the large grain size in these samples, each EBSD scan can only catch less than 20 grains. Nevertheless, the grain sizes are in the same order measured by both techniques. Considered the long sample preparation time (~ 2-4 hours) including cutting, setting in epoxy, grinding and polishing before the samples are ready for EBSD analysis, laser acoustic measurement therefore can serve as an alternative to provide a fast (1-5 minutes), NDT preliminary analysis of samples' grain sizes. Such fast analysis would shorten the turn-around-time to evaluate the effectiveness of surface treatment for process optimization.

5. Conclusions

In this study, a laser ultrasonic method was developed to measure residual stress profile and grain size in titanium alloy (Ti64) samples. The samples were subjected to shot peened at different temperatures ranging from 32 °C to 300 °C. Using the acoustoelastic constant, ultrasonic wave velocity approach was employed to measure the residual stress profiles. The in-depth distributions of residual stresses in the surface treated layer were investigated by the proposed method, X-ray stress measurement and center-hole drilling (CHD). The microstructures of the samples were investigated by using electron backscattering diffraction (EBSD) analysis.

The maximum CRS has increased from −127.11 MPa in the as-received sample to −698.03 after shot peening (300 °C). For the peened sample at 300 °C, the laser ultrasonic method estimated the CRS value as −698.03 MPa, while the X-ray and CHD methods yielded values of −556.375 MPa and −667.03 MPa, respectively. Additionally, a linear relationship between the centroid frequency ratio of two successive propagation distances and the mean grain size was observed. Although the grain size calculated by the proposed method has some degree of discrepancy (38 ~ 60%) compared to the results from EBSD measurement, it detects the grains size at the same order of magnitude as that by EBSD and there is certainly a room for further improvement. Being able to extract both residual stress and grain size information from a single measurement, the proposed laser ultrasonic method remains very promising for industrial applications as it is rapid, nondestructive, non-contact and ready for wide deployment.

CRediT authorship contribution statement

Santhakumar Sampath: Conceptualization, Methodology, Writing – original draft. **Zheng Zhang:** Resources, Writing – review & editing. **Zi Wen Tham:** Acquisition of data. **Yi Fan Chen:** Acquisition of data. **Thulsiram Gantala:** Analysis of data. **Debbie Hwee Leng Seng:** SEM analysis. **Lei Zhang:** Conceptualization, Writing – review & editing, Supervision.

Declaration of competing interest

The authors declare that they have no known competing financial interests or personal relationships that could have appeared to influence the work reported in this paper.

Acknowledgement

This research is supported by the Singapore National Research Foundation under its Central GAP Fund (Grant Reference NRF2020NRF-CG001-035, Project No. SC25/21-706317).

Appendix A. Damage model of shot-peening treated sample

The impact of shots on the sample causes plastic deformation, resulting in CRS, GR, dislocation, and other types of damage [76]. The formation of residual stress and grain size due to the peening process can significantly alter the elastic modulus [77]. The crystal lattice arrangement beneath the treated surface layer remains unchanged, and the elastic modulus is assumed to be unchanged. The cross-section of surface layers consists of plastic deformation, elastic deformation followed by the bulk material (left side of Fig. A1). Therefore, the damage model of the treated sample can be simplified as a two-layer model (right of Fig. A1). We assume that the surface treated layer is homogeneous and elastic within the measuring range.

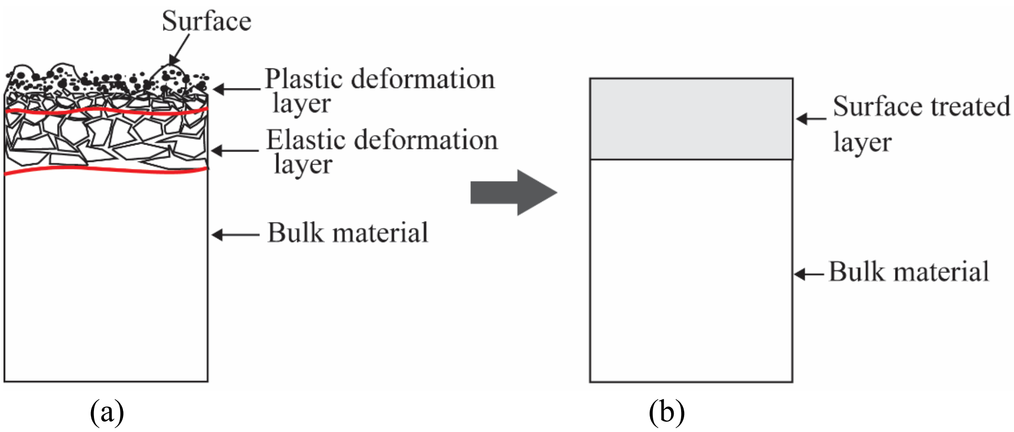

Figure A12. (Left) Damage model of shot-peening treated sample and (right) its simplified model.

Appendix B. Residual stress profile measurement

The residual stress of the material influences the propagation characteristics of the SAW, such as wave propagation time. Therefore, the method of calculating residual stress by measuring the SAW velocity used is based on the acoustoelastic theory [53, 78]. Assuming that SAW propagates through a nonlinear, homogeneous, and elastic material, the equation of SAW motion can be expressed as follows [79]:

$$\frac{\partial \sigma_{ij}}{\partial a_j} = \rho \frac{\partial^2 u_i}{\partial t^2} \quad \text{(B1)}$$

where σ_{ij} denotes the stress tensor, ρ is the material density, u is the particle displacement, a is the position vector, and t is the time. The residual stresses lead to a relationship between the first Piola–Kirchhoff stresses, σ_{ij}, and the displacement gradients, u_i, as

$$\sigma_{ij} = \sigma_{ij}^0 + A_{ijkl}\frac{\partial u_k}{\partial a_l} + \frac{1}{2}A_{ijklmn}\frac{\partial u_k}{\partial a_l}\frac{\partial u_m}{\partial a_n} + \cdots \quad \text{(B2)}$$

where σ_{ij}^0 is the residual stress in the material. A_{ijkl} and A_{ijklmn} denote the Huang coefficients [80] and are related to the elastic constants of the material by

$$A_{ijkl} = \sigma_{jl}^0 \delta_{ik} + \bar{C}_{ijkl}$$
$$A_{ijklmn} = \tilde{C}_{ijklmn} + \bar{C}_{jlmn}\delta_{ik} + \bar{C}_{ijnl}\delta_{km} + \bar{C}_{jnkl}\delta_{im} \tag{B3}$$

Here, δ is the Kronecker delta function and $\bar{C}$ and $\tilde{C}$ represent the elastic constants. Equation (B1) illustrates that the residual stress is a complex function of SAW velocity and is influenced by the elastic constants. Therefore, the relationship between residual stress and SAW velocity is not practically feasible for measuring the residual stress profile. In this study, the following steps are presented to simplify the relationship between residual stress and SAW velocity. The propagation of one-dimensional SAW in an intact sample (i.e., without WSP) can be expressed as

$$\rho(V_{11}^r)^2 = \lambda + 2\mu \tag{B4}$$

where λ and μ are Lamè elastic constants and V_{11}^r represent the SAW velocity of intact sample. By substituting Eqs. (B4) and (B2) into Eq. (B1), the SAW velocity (V_{11}) of peened sample can be obtained as [81]

$$V_{11}^2 = (V_{11}^r)^2(K_{11}\sigma_{11}^0 + K_{12}\sigma_{12}^0 + 1) \tag{B5}$$

where K_{11} and K_{12} are the acoustoelastic constants related to the material properties. σ_{11}^0 and σ_{12}^0 represent the residual stress in the x and y directions. When $K_{11} \gg K_{12}$, the relationship between the relative variation of the SAW velocity and residual stress (σ_{11}^0) can be expressed as follows [70, 82]:

$$\frac{V_{11} - V_{11}^r}{V_{11}^r} = \frac{\Delta V_{11}}{V_{11}^r} = K_{11}\sigma_{11}^0 \tag{B6}$$

where

$$K_{11} = \frac{1}{3\lambda + 2\mu}\left[\left(\frac{4\lambda + 10\mu + 4m}{\mu}\right) + \left(\frac{2l - 3\lambda - 10\mu - 4n}{\lambda + 2\mu}\right)\right] \quad \text{(B7)}$$

and l, m and n are the third-order elastic constants of the material. From Eq. (B6), it is noticed that the difference in SAW velocity is a function of the residual stress. When both the stress and the SAW propagation velocity are calculated, it becomes feasible to determine the acoustoelastic constants [70]. For example, if the stress is 600 MPa, the corresponding K_{11} is approximately 10^6 MPa^{-1}. By measuring the SAW velocity and knowing the acoustoelastic constants of the material, the residual stress can be computed using Eq. (B6).

Appendix C. Frequency shift-based grain size measurements

The propagation of the SAW through a peened sample causes the attenuation, which is influenced by the grain size. Studies have shown that the amplitude of SAW deceases as $1/x$, where x is the propagation distance [42,43]. Since the power of SAW exhibits a proportional relationship with frequency raised to the power of "n" and mean grain size raised to the power of "$(n-1)$", the scattering attenuation of SAW can be expressed as [51]

$$\alpha(f) = c\bar{d}^{n-1}f^{n} \quad \text{(C1)}$$

where $\alpha(f)$ is the attenuation in the frequency domain, n is exponential coefficient that depends on the scattering regimes ($0 \leq n \leq 4$), c represents a material coefficient that depends on the elastic constants and density of the material, and $\bar{d}$ is the mean grain size. When the SAW propagates for a distance of x and undergoes amplitude attenuation, the spectral magnitude of the incident SAW can be written as

$$|M(f)| = A_c e^{\left[-\frac{(f-f_c)^2}{2\sigma_c^2} - (b\bar{d}^{n-1})x\right]} \quad \text{(C2)}$$

where A_c and σ_c^2 are the amplitude and the variance of the SAW spectrum at the center frequency, f_c, respectively. b is the material constant. Assuming that the incident pulse has Gaussian shape, Eq. (C2) can be simplified as [44,45].

$$|M(f)| = A_c e^{\left[-\frac{(f-f_c)^2}{2\sigma_c^2}\right]} \quad \text{(C3)}$$

The ratio of the center frequencies between the two successive propagation distances is written as:

$$\frac{f_{c1}}{f_{c2}} = 1 + \frac{2\sigma_c^2 \alpha_o (x_2 - x_1)}{2\sigma_c^2 \alpha_o x_1 + 1} \quad \text{(C4)}$$

where f_{c1} and f_{c2} are the center frequencies at positions x_1 and x_2, respectively. Based on the linear relationship of $\alpha_o = b\bar{d}$, the mean grain size can be derived as

$$\bar{d} = \frac{f_{c1}/f_{c2} - 1}{2b\sigma_c^2 (x_2 - x_1)} \quad \text{(C5)}$$

Eq. (C5) provides an explicit formula for estimating the mean grain size based on the center frequency ratio between the two successive propagation distances in peened samples.

References

[1] G. Ongtrakulkij, A. Khantachawana, K. Kondoh, Effects of media parameters on enhance ability of hardness and residual stress of Ti6Al4V by fine shot peening, Surfaces and Interfaces, 18 (2020) 100424.
[2] Y. Guo, G. Liu, T. Jiao, X. Hu, H. Zhang, M. Liu, Creep-fatigue damage behavior of a titanium alloy at room temperature: Experiments and modeling, International Journal of Mechanical Sciences, 245 (2023) 108135.
[3] R. Julien, V. Velay, V. Vidal, Y. Dahan, R. Forestier, F. Rezai-Aria, Characterization and modeling of forged Ti-6Al-4V Titanium alloy with microstructural considerations during quenching process, International Journal of Mechanical Sciences, 142 (2018) 456-467.
[4] E. Maleki, O. Unal, M. Guagliano, S. Bagherifard, The effects of shot peening, laser shock peening and ultrasonic nanocrystal surface modification on the fatigue strength of Inconel 718, Materials Science and Engineering: A, 810 (2021) 141029.
[5] X. Nie, W. He, L. Zhou, Q. Li, X. Wang, Experiment investigation of laser shock peening on TC6 titanium alloy to improve high cycle fatigue performance, Materials Science and Engineering: A, 594 (2014) 161-167.
[6] B. Wang, L. Zhou, Y. Cao, P. Xue, L. Wu, Analysis of residual stress relief for Ti62A alloy welded joints by post weld heat treatment considering creep effect, Journal of Materials Research and Technology, 24 (2023) 7462-7474.
[7] E. Maleki, O. Unal, K. Reza Kashyzadeh, Efficiency analysis of shot peening parameters on variations of hardness, grain size and residual stress via Taguchi approach, Metals and Materials International, 25 (2019) 1436-1447.
[8] L. Bao, K. Li, J. Zheng, Y. Zhang, K. Zhan, Z. Yang, B. Zhao, V. Ji, Surface characteristics and stress corrosion behavior of AA 7075-T6 aluminum alloys after different shot peening processes, Surface and Coatings Technology, 440 (2022) 128481.

[9] S. Agaram, S.M. Srinivasan, A.K. Kanjarla, Crystal plasticity modelling of stability of residual stresses induced by shot peening, International Journal of Mechanical Sciences, 230 (2022) 107526.
[10] L. Wang, L. Zhou, L. Liu, W. He, X. Pan, X. Nie, S. Luo, Fatigue strength improvement in Ti-6Al-4V subjected to foreign object damage by combined treatment of laser shock peening and shot peening, International Journal of Fatigue, 155 (2022) 106581.
[11] S.-L. Yao, G.-Y. Wang, H. Yu, J. Wang, K.-S. Li, S. Liu, X.-C. Zhang, S.-T. Tu, Influence of submerged micro-abrasive waterjet peening on surface integrity and fatigue performance of TA19 titanium alloy, International Journal of Fatigue, 164 (2022) 107076.
[12] W.L. Chan, H.K.F. Cheng, Hammer peening technology—the past, present, and future, The International Journal of Advanced Manufacturing Technology, (2022) 1-19.
[13] Z.-C. Huang, Z.-J. Zhou, Y.-Q. Jiang, Effect of shot peening on static and fatigue properties of self-piercing riveting joints, Journal of Materials Research and Technology, 18 (2022) 1070-1080.
[14] H.-L. Yao, X.-Z. Hu, Z.-H. Yi, J. Xia, X.-Y. Tu, S.-B. Li, B. Yu, M.-X. Zhang, X.-B. Bai, Q.-Y. Chen, Microstructure and improved anti-corrosion properties of cold-sprayed Zn coatings fabricated by post shot-peening process, Surface and Coatings Technology, 422 (2021) 127557.
[15] J. Zhao, J. Tang, H. Ding, W. Shao, X. Zhao, H. Liu, T. Jiang, A numerical and experimental investigation on the evolution of three-dimensional surface topography of 12Cr2Ni4A steel in shot peening, Journal of Manufacturing Processes, 70 (2021) 259-270.
[16] E. Maleki, O. Unal, A. Amanov, Novel experimental methods for the determination of the boundaries between conventional, severe and over shot peening processes, Surfaces and Interfaces, 13 (2018) 233-254.
[17] S. Bagherifard, S. Slawik, I. Fernández-Pariente, C. Pauly, F. Mücklich, M. Guagliano, Nanoscale surface modification of AISI 316L stainless steel by severe shot peening, Materials & Design, 102 (2016) 68-77.
[18] J. Wu, H. Liu, P. Wei, Q. Lin, S. Zhou, Effect of shot peening coverage on residual stress and surface roughness of 18CrNiMo7-6 steel, International Journal of Mechanical Sciences, 183 (2020) 105785.
[19] S. Aguado-Montero, C. Navarro, J. Vázquez, F. Lasagni, S. Slawik, J. Domínguez, Fatigue behaviour of PBF additive manufactured TI6AL4V alloy after shot and laser peening, International Journal of Fatigue, 154 (2022) 106536.
[20] S. Spanrad, J. Tong, Characterisation of foreign object damage (FOD) and early fatigue crack growth in laser shock peened Ti–6Al–4V aerofoil specimens, Materials Science and Engineering: A, 528 (2011) 2128-2136.
[21] Y. Harada, K. Mori, Effect of processing temperature on warm shot peening of spring steel, Journal of materials processing technology, 162 (2005) 498-503.
[22] S.H. Lim, Z. Zhang, D.H.L. Seng, M. Lin, S.L. Teo, F. Wei, A.K.H. Cheong, S. Wang, J. Pan, In-situ warm shot peening on Ti-6Al-4V alloy: effects of temperature on fatigue life, residual stress, microstructure and mechanical properties, Journal of Alloys and Compounds, 882 (2021) 160701.
[23] J. Zhao, J. Tang, W. Zhou, T. Jiang, H. Liu, B. Xing, Numerical modeling and experimental verification of residual stress distribution evolution of 12Cr2Ni4A steel generated by shot peening, Surface and Coatings Technology, 430 (2022) 127993.
[24] S. Sunny, R. Mathews, H. Yu, A. Malik, Effects of microstructure and inherent stress on residual stress induced during powder bed fusion with roller burnishing, International Journal of Mechanical Sciences, 219 (2022) 107092.
[25] M.-N. Avettand-Fènoël, T. Sapanathan, T. Pirling, G. Racineux, A. Simar, J.-M. Drezet, Investigation of residual stresses in planar dissimilar magnetic pulse welds by neutron diffraction, Journal of Manufacturing Processes, 68 (2021) 1758-1766.
[26] C. Shen, M. Reid, K.-D. Liss, Z. Pan, Y. Ma, D. Cuiuri, S. van Duin, H. Li, Neutron diffraction residual stress determinations in Fe3Al based iron aluminide components fabricated using wire-arc additive manufacturing (WAAM), Additive Manufacturing, 29 (2019) 100774.
[27] H. Liu, Y. Wei, C.K.I. Tan, D.T. Ardi, D.C. Tan, C.J. Lee, XRD and EBSD studies of severe shot peening induced martensite transformation and grain refinements in austenitic stainless steel, Materials Characterization, 168 (2020) 110574.
[28] F. Yin, X. Zhang, F. Chen, S. Hu, K. Ming, J. Zhao, L. Xie, Y. Liu, L. Hua, J. Wang, Understanding the microstructure refinement and mechanical strengthening of dual-phase high entropy alloy during ultrasonic shot peening, Materials & Design, 227 (2023) 111771.
[29] M. Olson, A. DeWald, M. Hill, Precision of hole-drilling residual stress depth profile measurements and an updated uncertainty estimator, Experimental Mechanics, 61 (2021) 549-564.
[30] G. Jiang, F. Haiyang, P. Bo, K. Renke, Recent progress of residual stress measurement methods: A review, Chinese Journal of Aeronautics, 34 (2021) 54-78.

[31] Z. Liu, B. Lin, X. Liang, A. Du, Numerical simulation of laser-generated Rayleigh wave pulses propagation in the machined surface with residual stress using finite-difference method, Optik, 248 (2021) 168072.
[32] J. Goulmy, P. Kanoute, E. Rouhaud, L. Toualbi, S. Kruch, V. Boyer, J. Badreddine, D. Retraint, A calibration procedure for the assessment of work hardening Part II: Application to shot peened IN718 parts, Materials Characterization, 175 (2021) 111068.
[33] T.M. Tien, N.V. Phoi, L.A. Tuyen, L.L. Nguyen, Study of strain and residual stress distribution in the thickness direction by layer removal method and X-ray diffraction, in: 2016 3rd International Conference on Green Technology and Sustainable Development (GTSD), IEEE, 2016, pp. 155-160.
[34] J. Holmberg, J. Berglund, A. Stormvinter, P. Andersson, P. Lundin, Influence of Local Electropolishing Conditions on Ferritic–Pearlitic Steel on X-Ray Diffraction Residual Stress Profiling, Journal of Materials Engineering and Performance, (2023) 1-9.
[35] P. Lopez-Ruiz, M. Garcia-Blanco, G. Vara, I. Fernández-Pariente, M. Guagliano, S. Bagherifard, Obtaining tailored surface characteristics by combining shot peening and electropolishing on 316L stainless steel, Applied Surface Science, 492 (2019) 1-7.
[36] S. Breumier, F. Adamski, J. Badreddine, M. Lévesque, G. Kermouche, Microstructural and mechanical characterization of a shot peening induced rolled edge on direct aged Inconel 718 alloy, Materials Science and Engineering: A, 816 (2021) 141318.
[37] X. Yue, S. Hu, X. Wang, Y. Liu, F. Yin, L. Hua, Understanding the nanostructure evolution and the mechanical strengthening of the M50 bearing steel during ultrasonic shot peening, Materials Science and Engineering: A, 836 (2022) 142721.
[38] H. Pan, Z. Wang, B. Zhang, P. Jiang, Z. Wang, W. Wu, L. Liu, J. Li, Z. Wu, Z. Cai, Effect of Shot Peening on Microstructure and Mechanical Properties of 316L Stainless Steel Prepared by 3D Printing with Different Forming Angles, Journal of Materials Engineering and Performance, (2023) 1-10.
[39] R. Patel, W. Li, R.J. Smith, S.D. Sharples, M. Clark, Orientation imaging of macro-sized polysilicon grains on wafers using spatially resolved acoustic spectroscopy, Scripta Materialia, 140 (2017) 67-70.
[40] T. Owoseni, M. Bai, N. Curry, E. Lester, D. Grant, T. Hussain, Residual stress measurement of suspension HVOF-sprayed alumina coating via a hole-drilling method, Journal of Thermal Spray Technology, 29 (2020) 1339-1350.
[41] Z. Zhang, Q. Tan, Y. Cui, Y. Tian, Y. Wang, H. Qin, Z. Bi, Y. Wang, Experimental validation of residual stress thermomechanical simulation in as-quenched superalloy discs by using diffraction and incremental hole-drilling methods, Materials Today Communications, 27 (2021) 102229.
[42] Y. Peng, J. Zhao, L.-s. Chen, J. Dong, Residual stress measurement combining blind-hole drilling and digital image correlation approach, Journal of Constructional Steel Research, 176 (2021) 106346.
[43] T. Wu, S. Degener, S. Tinkloh, A. Liehr, W. Zinn, J. Nobre, T. Tröster, T. Niendorf, Characterization of residual stresses in fiber metal laminate interfaces–A combined approach applying hole-drilling method and energy-dispersive X-ray diffraction, Composite Structures, 299 (2022) 116071.
[44] C. Barile, S. Carone, C. Casavola, G. Pappalettera, Implementation of Gaussian Process Regression to strain data in residual stress measurements by hole drilling, Measurement, 211 (2023) 112590.
[45] M. Alinaghian, I. Alinaghian, M. Honarpisheh, Residual stress measurement of single point incremental formed Al/Cu bimetal using incremental hole-drilling method, International Journal of Lightweight Materials and Manufacture, 2 (2019) 131-139.
[46] F. Kümmel, A. Magnier, T. Wu, T. Niendorf, H.W. Höppel, Residual Stresses in Ultrafine-Grained Laminated Metal Composites Analyzed by X-ray Diffraction and the Hole-Drilling Method, Advanced Engineering Materials, 24 (2022) 2200274.
[47] H. Liu, Y. Li, T. Li, X. Zhang, Y. Liu, K. Liu, Y. Wang, Influence factors analysis and accuracy improvement for stress measurement using ultrasonic longitudinal critically refracted (LCR) wave, Applied Acoustics, 141 (2018) 178-187.
[48] J. He, Z. Li, J. Teng, M. Li, Y. Wang, Absolute stress field measurement in structural steel members using the Lcr wave method, Measurement, 122 (2018) 679-687.
[49] F. Dong, X. Wang, Q. Yang, A. Yin, X. Xu, Directional dependence of aluminum grain size measurement by laser-ultrasonic technique, Materials Characterization, 129 (2017) 114-120.
[50] B. Hutchinson, B. Moss, A. Smith, A. Astill, C. Scruby, G. Engberg, J. Björklund, Online characterisation of steel structures in hot strip mill using laser ultrasonic measurements, Ironmaking & steelmaking, 29 (2002) 77-80.
[51] R. Xue, X. Wang, Q. Yang, F. Dong, Y. Zhang, J. Cao, G. Song, Grain size characterization of aluminum based on ensemble empirical mode decomposition using a laser ultrasonic technique, Applied Acoustics, 156 (2019) 378-386.

[52] R. Sanderson, Y. Shen, Measurement of residual stress using laser-generated ultrasound, International journal of pressure vessels and piping, 87 (2010) 762-765.
[53] M. Duquennoy, M. Ouaftouh, M. Qian, F. Jenot, M. Ourak, Ultrasonic characterization of residual stresses in steel rods using a laser line source and piezoelectric transducers, Ndt & E International, 34 (2001) 355-362.
[54] A. Moreau, C.S. Man, Laser-Ultrasonic Measurements of Residual Stresses in a 7075-T651 Aluminum Sample Surface-Treated with Low Plasticity Burnishing, in: AIP Conference Proceedings, American Institute of Physics, 2006, pp. 1434-1441.
[55] A. Ruiz M, P.B. Nagy, Diffraction correction for precision surface acoustic wave velocity measurements, The Journal of the Acoustical Society of America, 112 (2002) 835-842.
[56] P. Hu, J.A. Turner, Transverse-to-transverse diffuse ultrasonic scattering, The Journal of the Acoustical Society of America, 142 (2017) 1112-1120.
[57] E. Lindh-Ulmgren, M. Ericsson, D. Artymowicz, W.B. Hutchinson, Laser-ultrasonics as a technique to study recrystallisation and grain growth, in: Materials Science Forum, Trans Tech Publ, 2004, pp. 1353-1362.
[58] X. Bai, B. Tie, J.-H. Schmitt, D. Aubry, Finite element modeling of grain size effects on the ultrasonic microstructural noise backscattering in polycrystalline materials, Ultrasonics, 87 (2018) 182-202.
[59] T. Garcin, J.H. Schmitt, M. Militzer, In-situ laser ultrasonic grain size measurement in superalloy INCONEL 718, Journal of alloys and compounds, 670 (2016) 329-336.
[60] J. Fan, F. Wang, H. Cui, W. Wang, Concentration determination in a cylinder-simulated gas–solid two phase flow using ultrasonic backscattering method, Applied Acoustics, 203 (2023) 109212.
[61] Y. Anmin, Y. Quan, H. Fei, W. Xiaochen, D. Feng, W. Yanlong, S. Xuedao, Grain Size Measurement in Low Carbon Steel Sheets by Laser Ultrasonics, Journal of Mechanical Engineering, 53 (2017) 11-19.
[62] X.-G. Zhang, W. Simpson Jr, J. Vitek, D. Barnard, L. Tweed, J. Foley, Ultrasonic attenuation due to grain boundary scattering in copper and copper-aluminum, The Journal of the Acoustical Society of America, 116 (2004) 109-116.
[63] X. Bai, Y. Zhao, J. Ma, R. Guo, H. Zhang, Grain size characterization by laser-based ultrasonics based on the centroid frequency shift method, Materials Characterization, 155 (2019) 109800.
[64] R. Xue, X. Wang, Q. Yang, D. Xu, Y. Sun, J. Zhang, S. Krishnaswamy, Grain size distribution characterization of aluminum with a particle swarm optimization neural network using laser ultrasonics, Applied Acoustics, 180 (2021) 108125.
[65] J. Zhang, D. Xu, X. Wang, J. Zhao, H. He, Q. Yang, Grain size characterization method of dual-phase titanium alloys with complex microstructure based on laser ultrasonic, Measurement, 211 (2023) 112670.
[66] S. Sampath, H. Sohn, Non-contact microcrack detection via nonlinear Lamb wave mixing and laser line arrays, International Journal of Mechanical Sciences, 237 (2023) 107769.
[67] K. Zhang, S. Li, Z. Zhou, Detection of disbonds in multi-layer bonded structures using the laser ultrasonic pulse-echo mode, Ultrasonics, 94 (2019) 411-418.
[68] E. Hu, Y. He, Y. Chen, Experimental study on the surface stress measurement with Rayleigh wave detection technique, Applied Acoustics, 70 (2009) 356-360.
[69] H. Hu, Z. Zou, Y. Jiang, X. Wang, K. Yi, Finite element simulation and experimental study of residual stress testing using nonlinear ultrasonic surface wave technique, Applied Acoustics, 154 (2019) 11-17.
[70] Y. Zhan, C. Liu, X. Kong, Z. Lin, Experiment and numerical simulation for laser ultrasonic measurement of residual stress, Ultrasonics, 73 (2017) 271-276.
[71] S. Zhang, X. Li, H. Jeong, H. Hu, Experimental investigation of material nonlinearity using the Rayleigh surface waves excited and detected by angle beam wedge transducers, Ultrasonics, 89 (2018) 118-125.
[72] M. Liu, J.-Y. Kim, L. Jacobs, J. Qu, Experimental study of nonlinear Rayleigh wave propagation in shot-peened aluminum plates—Feasibility of measuring residual stress, Ndt & E International, 44 (2011) 67-74.
[73] M. Keyvani, T. Garcin, M. Militzer, D. Fabregue, Laser ultrasonic measurement of recrystallization and grain growth in an L605 cobalt superalloy, Materials Characterization, 167 (2020) 110465.
[74] L. Peral, A. Zafra, S. Bagherifard, M. Guagliano, I. Fernández-Pariente, Effect of warm shot peening treatments on surface properties and corrosion behavior of AZ31 magnesium alloy, Surface and Coatings Technology, 401 (2020) 126285.
[75] T. Sakai, A. Belyakov, R. Kaibyshev, H. Miura, J.J. Jonas, Dynamic and post-dynamic recrystallization under hot, cold and severe plastic deformation conditions, Progress in materials science, 60 (2014) 130-207.
[76] E. Maleki, G.H. Farrahi, K. Reza Kashyzadeh, O. Unal, M. Gugaliano, S. Bagherifard, Effects of conventional and severe shot peening on residual stress and fatigue strength of steel AISI 1060 and residual stress relaxation due to fatigue loading: Experimental and numerical simulation, Metals and Materials International, 27 (2021) 2575-2591.

[77] H. Li, H. Wang, R. Alderliesten, J. Xiang, Y. Lin, Y. Xu, H. Zhao, J. Tao, The residual stress characteristics and mechanical behavior of shot peened fiber metal laminates based on the aluminium-lithium alloy, Composite Structures, 254 (2020) 112858.
[78] M. Doxbeck, M.A. Hussain, J. Frankel, A. Abbate, Use of laser generated creeping longitudinal waves to determine residual stresses, in: 2000 IEEE Ultrasonics Symposium. Proceedings. An International Symposium (Cat. No. 00CH37121), IEEE, 2000, pp. 725-728.
[79] B. Zhong, J. Zhu, Measurement of third-order elastic constants using thermal modulation of ultrasonic waves, Applied Physics Letters, 118 (2021) 261903.
[80] J.H. Cantrell, Substructural organization, dislocation plasticity and harmonic generation in cyclically stressed wavy slip metals, Proceedings of the Royal Society of London. Series A: Mathematical, Physical and Engineering Sciences, 460 (2004) 757-780.
[81] Z. Li, J. He, J. Teng, Y. Wang, Internal stress monitoring of in-service structural steel members with ultrasonic method, Materials, 9 (2016) 223.
[82] M. Ya, P. Marquette, F. Belahcene, J. Lu, Residual stresses in laser welded aluminium plate by use of ultrasonic and optical methods, Materials Science and Engineering: A, 382 (2004) 257-264.